In situ microstructural evolution in face-centered and body-centered cubic complex concentrated solid-solution alloys under heavy ion irradiation

Calvin Parkin^a

cparkin@wisc.edu, ph: 1-859-533-3650

Michael Moorehead^a, Mohamed Elbakhshwan^a, Kumar Sridharan^a, Adrien Couet^a

moorehead2@wisc.edu, elbakhshwan@wisc.edu, kumar.sridharan@wisc.edu, couet@wisc.edu

^aUniversity of Wisconsin- Madison, 1500 Engineering Drive, Madison, WI 53706

Jing Hu^b, Wei-Ying Chen^b, Meimei Li^b

hujing0321@gmail.com, wychen@anl.gov, mli@anl.gov bArgonne National Laboratory, 9700 Cass Avenue, Lemont, IL 60439

Lingfeng He^c

lingfeng.he@inl.gov cIdaho National Laboratory, 1955 N. Fremont Ave., Idaho Falls, ID 83415

Abstract

This study characterizes the microstructural evolution of single-phase complex concentrated solid-solution alloy (CSA) compositions under heavy ion irradiation with the goal of evaluating mechanisms for CSA radiation tolerance in advanced fission systems. Three such alloys, Cr₁₈Fe₂₇Mn₂₇Ni₂₈, Cr₁₅Fe₃₅Mn₁₅Ni₃₅, and equimolar NbTaTiV, along with reference materials (pure Ni and E90 for the CrFeMnNi family and pure V for NbTaTiV) were irradiated at 50 K and 773 K with 1 MeV Kr⁺⁺ ions to various levels of displacements per atom (dpa) using in-situ transmission electron microscopy. Cryogenic irradiation resulted in small defect clusters and faulted dislocation loops as large as 12 nm in face-centered cubic (FCC) CSAs. With thermal diffusion suppressed at cryogenic temperatures, defect densities were lower in all CSAs than in their less compositionally complex reference materials indicating that point defect production is reduced during the displacement cascade stage. High temperature irradiation of the two FCC CSA resulted in the formation of interstitial dislocation loops which by 2 dpa grew to an average

size of 27 nm in Cr₁₈Fe₂₇Mn₂₇Ni₂₈ and 10 nm in Cr₁₅Fe₃₅Mn₁₅Ni₃₅. This difference in loop growth kinetics was attributed to the difference in Mn-content due to its effect on the nucleation rate by increasing vacancy mobility or reducing the stacking-fault energy.

Keywords: irradiation effect, ion irradiation, in situ transmission electron microscopy, complex concentrated solid-solution alloy, cryogenic temperature

1. Introduction

Fast-reactor cladding and ducts require alloys that are resistant to void swelling up to several hundreds of displacements per atom (dpa), maintain adequate creep strength up to 650 °C and fracture toughness at 320 °C or less, and exhibit strong corrosion resistance in liquid sodium or liquid lead-alloy coolants. Because of unacceptable levels of void swelling in 316 stainless steel, the focus for cladding and duct applications has been ferritic-martensitic (F-M) steels. Based on corrosion resistance, fracture toughness, and void swelling considerations, 9Cr steel has been favored over HT9 for the next generation cladding and duct application for fast reactors. Further optimization led to the consideration of compositionally optimized austenitic alloys such as D9 as well as G92 ferritic-martensitic steels [1, 2]. On account of its austenitic structure, D9 is not expected to have adequate swelling resistance after hundreds of dpa while HT9 and G92 have not been tested in excess of 200 dpa [3] and have shown a dramatic decrease in mechanical properties after testing in liquid Na at 650 °C [4]. In addition, HT9 has limited resistance to creep and creep fatigue above 550 °C [5]. Oxide dispersion strengthened (ODS) ferritic-martensitic steels show promise [2], but fabrication of claddings of this material at reasonable cost in sufficient volumes, and with predictable and reproducible properties continues to be a significant challenge. Overall, the deployment of fast reactors is currently limited partly by the development of materials which can sustain radiation damage at high levels of dpa to meet the necessary safety and economic criteria for licensing and commercialization. It is therefore necessary to explore new alloy compositional designs, outside the paradigms of ferritic and austenitic steels, such as high-entropy alloys (HEAs). HEAs represent a radical departure from traditional alloy design, which has historically involved a single principle alloying element with small additions (<20 at% of alloying elements) to tailor corrosion or mechanical properties [6]. HEAs typically consist of four or more elements, with no single element having a concentration less than 5 at% or higher than 35 at%, which may lead to a random configuration of atoms on lattice sites [7, 8]. If the configurational entropy is sufficient to stabilize a single phase, the alloy may be considered a CSA (complex concentrated solid-solution alloy) [9, 10]. However, even in a single-phase CSA the configuration may not be entirely random, as it has been shown that short range chemical order in HEAs may also drive the stability of a single phase [11-13]. CSAs based on 3d transition metals (FCC) and light refractory metals (BCC) exhibit strength comparable to SS316 and Inconel 718, respectively, and with acceptable ductility [7, 14]. CSAs composed of various refractory metals, such as TiVTa-based alloys, have shown good compressive strength at high temperature and acceptable tensile ductility at room temperature [15].

In addition, atomistic modeling and experiments suggest that certain CSA compositions possess inherent resistance to radiation damage effects, such that CSAs may show potential for replacement of conventional alloys, or at least their base matrices, in nuclear systems. It is well understood that microstructural changes under irradiation are driven by point defect accumulation and influenced by the spatial distribution and mobility of individual point defects and defect clusters after the end of a damage cascade. CSAs were first believed to possess

intrinsic resistance to radiation damage owing to their highly disordered solid-solution matrix resulting in sluggish mass diffusion due to an inherently strained lattice, which would limit the densities of irradiation-induced 2D/3D defects [16]. While some CSAs have shown an increase in resistance to irradiation effects as function of compositional complexity, these properties are not simply dependent on the number of alloying elements and the resulting disorder, but rather on the interactions which take place between cascades, defect clusters, isolated defects, and sinks [6, 17-20]. Kumar et al. were able to show that the FCC CSA Cr₁₈Fe₂₇Mn₂₇Ni₂₈ experienced no swelling after 10 dpa Ni²⁺ ion irradiation at 700 °C [14]. Chen et al. showed that hardening effects and microstructural evolution as a function of dose in CoCrFeMnNi and Al_{0.3}CoCrFeNi were comparable to SS316H at 300 °C [21]. Li et al. also showed similar effects in Cr₁₈Fe₂₇Mn₂₇Ni₂₈ compared to conventional austenitic FeNiCr alloys under neutron irradiation [22]. This would suggest that compositional complexity influences radiation damage tolerance to a similar degree as alloying SS316 with Ti, Si, P, and native precipitates [23]. Beyond austenitic stainless steels, microstructural evolution of body-centered cubic (BCC) F-M steels under irradiation are detailed in [24], although these results are likely not entirely applicable to lightrefractory BCC HEA, especially those with a single phase. Light refractory CSAs are of interest because of their larger variation in atomic sizes and masses and therefore greater lattice distortion, as well as the inherent lower steady state swelling rate of the BCC structure. Increasing recombination within the displacement cascade or reducing single-defect or defectcluster mobility are proposed mechanisms to explain this radiation damage resistance [25-31]. However, experimental studies are needed to determine if the radiation resistance of CSAs is driven by different energy deposition during the thermal spike and/or different post-cascade

point defect mobility. Possible answers lie in the CSA microstructural evolution with irradiation dose and temperature.

This study focuses on the characterization of the microstructural evolution of multiple CSA compositions under heavy ion irradiation with the goal of identifying the active mechanisms which lead to radiation damage tolerance. Experiments were performed using in situ heavy ion irradiation under transmission electron microscope (TEM) at the Intermediate Voltage Electron Microscope (IVEM)-Tandem facility at Argonne National Laboratory (ANL), which allows for the evolution of the microstructure to be observed while maintaining precise control of dose, dose rate, imaging condition, and irradiation temperature. Selected compositions from the CrFeMnNi and NbTaTiV systems were irradiated in situ up to ~2 dpa at 50 K and 773 K and compared to structurally similar but less compositionally complex reference materials. The two experiment temperatures are intended to isolate the mechanisms which have been proposed to increase radiation resistance. At cryogenic temperatures thermal diffusion is strongly suppressed, causing point defects to remain more localized within the irradiation cascade instead of growing or migrating to sinks, giving a measure of the primary defect production from irradiation. This isolates mechanisms which solely reduce point defect production within the displacement cascade, as discussed in Section 4.1. At high temperature, point defects can diffuse and the effect of compositional complexity on the clustering behavior of defects can be investigated. Results are then discussed in the framework of these mechanisms.

2. Experimental Procedures

2.1 Alloy Selection

Three CSA compositions were investigated under various irradiation temperatures. Given compositions are in atomic percent. Pure Ni and Febal Ni₁₅Cr₁₆ model alloy E90 were used for reference against two face-centered cubic (FCC) CSAs: Cr₁₈Fe₂₇Mn₂₇Ni₂₈ and Cr₁₅Fe₃₅Mn₁₅Ni₃₅, while pure V was compared to the equimolar BCC CSA: NbTaTiV. The FCC CSA Cr₁₈Fe₂₇Mn₂₇Ni₂₈ is the same composition studied by Kumar *et al.* in [14] and was originally based off of Cantor's CoCrFeMnNi alloy, leaving Co out due to activation concerns and lowering Cr to slightly sub-equimolar concentration to stabilize a single phase after homogenization at 1200 °C for 48 hours [32]. CALPHAD calculations (shown Figure 1a.) predicted the formation of a new BCC phase in Cr₁₈Fe₂₇Mn₂₇Ni₂₈ below approximately 775 °C, and indeed phase separation did occur after annealing for 1000 hours at 700°C [33]. The Cr₁₅Fe₃₅Mn₁₅Ni₃₅ was one of very few compositions in the CrFeMnNi family which remained single phase down to at least 600 °C, as predicted by CALPHAD results shown in Figure 1b. A reduction in void swelling in austenitic FeNiCrMn alloys was correlated to an increase in Ni content, so this second CSA composition, with higher Ni, shows promise [34]. Because BCC materials tend to have lower void swelling resistance compared to FCC materials due to a lower steady state swelling rate, a BCC CSA was also selected [35, 36]. Alloys from the BCC system NbTaTiVZr were found to favor phase separation after slow cooling due to a tendency to form a Zr-rich hexagonal close-packed (HCP) phase, so Zr was lowered in favor of equimolar NbTaTiV [37]. NbTaTiV is predicted by CALPHAD to spinodally decompose into two BCC phases slightly above 500 °C as shown in Figure 1c. Although Cr₁₈Fe₂₇Mn₂₇Ni₂₈ and NbTaTiV are expected to phase separate at reactor temperatures, they are not expected (and, as detailed later,

have not been observed) to phase separate over the course of the irradiation experiment and thus remain suitable for studying the effect of compositional complexity on radiation resistance.

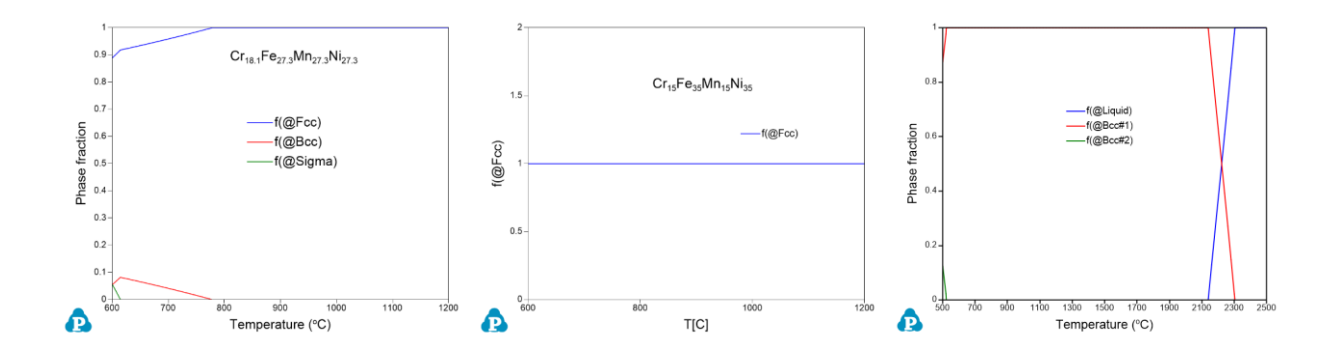


Figure 1. Predicted phase evolutions of a) $Cr_{18}Fe_{27}Mn_{27}Ni_{28}$ and b) $Cr_{15}Fe_{35}Mn_{15}Ni_{35}$ from 600 to 1200 °C. BCC phase is approximately $Cr_{72}Fe_{10}Mn_{18}$ and σ phase is tetragonal with $Cr_{45}Fe_{27}Mn_{27}Ni_2$. c) Phase evolution of NbTaTiV from 500 to 2500°C. 2^{nd} BCC phase has composition $Nb_{52}Ta_{18}Ti_{14}V_{16}$.

Table 1. Irradiated materials and their fabrication and processing methods. Materials were cast using either vacuum arc-melting (AM) or vacuum induction melting (VIM) and then annealed.

Material	Fabrication	Processing	Electro-polishing			
50 K Irradiation			Solution	Voltage [V]	Temp [°C]	
Ni	Foil received	Annealed by	5% perchloric	28	-40	
		vendor	acid in methanol			
E90 (FeCr16Ni15)	AM	Rolled to 0.2 mm	A2 electrolyte	17-18	-24	
		thickness, disks	(90 ml distilled			
		punched, annealed	water, 730 ml			
		under high	ethanol, 100 ml			
		vacuum for 30 min at 1050 °C	ethylene glycol monobutyl			
		mm at 1030 C	ether, and 78 ml			
			perchloric acid)			
$Cr_{18}Fe_{27}Mn_{27}Ni_{28}$	AM	Annealed 1200 °C	A2 electrolyte	17-18	-24	
-, -, -,		for 2 days	Ž			
$Cr_{15}Fe_{35}Mn_{15}Ni_{35}$	AM	Annealed 1200 °C	5% perchloric	28	-40	
		for 2 days	acid in methanol			
V	AM	Suction cast into	10% perchloric	26-28 V	-35	
		2mm diameter rod	acid in methanol	• 0	4.0	
NbTaTiV	VIM	Annealed 1200 °C	5% perchloric	20	-40	
		for 7 days	acid in methanol			
773 K Irradiation						
$\frac{775 \text{ Kindadion}}{\text{Cr}_{18}\text{Fe}_{27}\text{Mn}_{27}\text{Ni}_{28}}$	VIM	Annealed 1200 °C	5% perchloric	28	-40	
C1101 C2/111112/11128	, 21 71	for 2 days	acid in methanol	20	.0	
Cr ₁₅ Fe ₃₅ Mn ₁₅ Ni ₃₅	AM	Annealed 1200 °C	5% perchloric	28	-40	
10 00 101 100		for 2 days	acid in methanol		-	

2.2 Sample Preparation

Table 1 shows the fabrication and processing details for each material used in the irradiation experiments. Materials were cast using either vacuum arc-melting (AM) or vacuum induction-melting (VIM) and then annealed. The two FCC CSAs, Cr₁₈Fe₂₇Mn₂₇Ni₂₈ and Cr₁₅Fe₃₅Mn₁₅Ni₃₅, were arc-melted and tilt cast into a rod geometry using an Arcast Arc200 unit. The material was sectioned into 1- to 2-mm thick circular discs, ~10 mm in diameter, which were then encapsulated in a quartz tube for homogenization. E90 was also fabricated by vacuum arc-melting, after which it was rolled to sheets of 0.2-mm thickness from which disks were punched

before annealing. A VIM Cr₁₈Fe₂₇Mn₂₇Ni₂₈ sheet was also used for the high temperature irradiation. The refractory CSA, equimolar NbTaTiV, was fabricated by vacuum induction melting. Pure vanadium was used as a reference material. V samples were fabricated by arcmelting and suction casting into 2-mm diameter rods. All CSAs were finally annealed at temperatures and times necessary to obtain a homogeneous single-phase microstructure, followed by water quench. The single-phase microstructures of each alloy were confirmed by coupled θ -2 θ powder X-ray diffraction using a Bruker D8 Discover with a copper tube creating K_{α} X-rays of wavelength 1.54 Å. Zeiss LEO 1530 and JEOL JSM-6610 scanning electron microscopes (SEM) each equipped with Thermo Scientific UltraDry detectors were used to confirm the presence of equiaxed grains and compositional homogeneity. Illustrations of final grained microstructures and compositional homogeneity are shown in Figure 2. Some porosity is present from the arc melting but was easily avoided within the electron transparent area of an electropolished specimen. The chemistry of the final ingots was characterized using inert gas fusion (IGF), combustion infrared detection (CID), and direct current plasma emission spectroscopy (DCPES) techniques as well as inductively coupled plasma optical emission spectrometry (ICP-OES). Figure 2 shows SEM and EDS micrographs confirming grain structure and chemical homogeneity of arc-melted CSAs after homogenization in an inert environment. Table 2 shows the compositions of the samples analyzed and the respective techniques used for their analysis. The final alloy compositions were comparable to the targeted compositions, while the impurity levels were kept to less than a few tenths of an atomic percent.

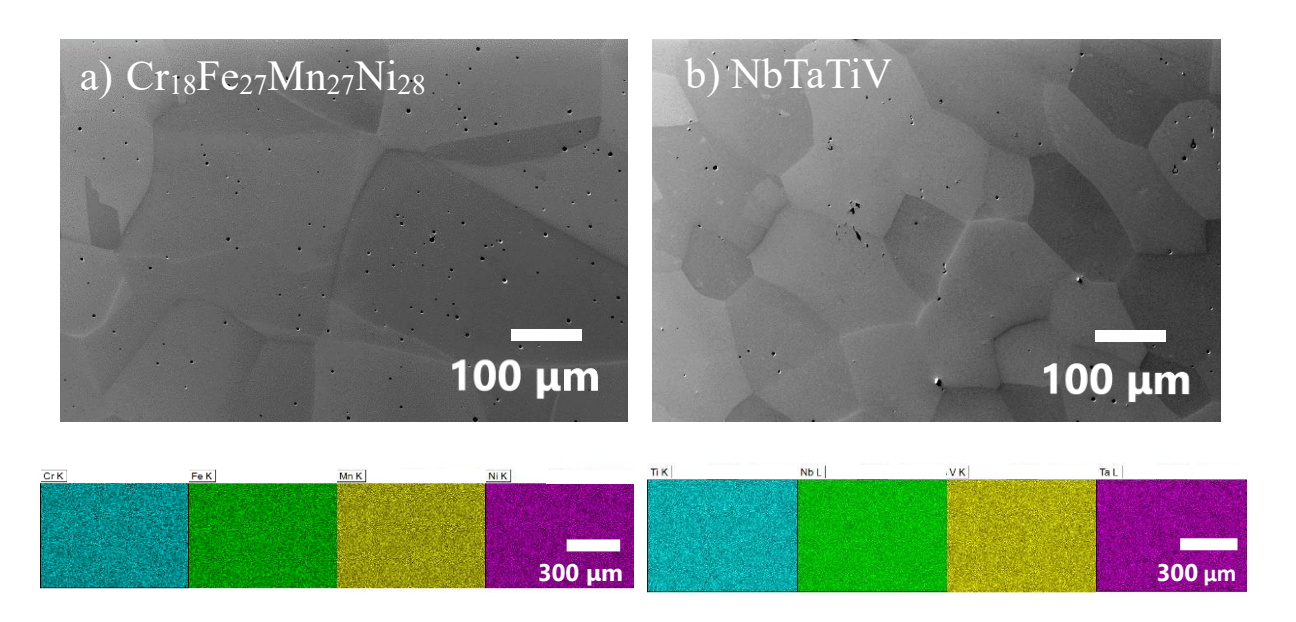


Figure 2. SEM and EDS micrographs confirming grain structure and chemical homogeneity of arc-melted CSAs after homogenization in an inert environment. a) Cr₁₈Fe₂₇Mn₂₇Ni₂₈ homogenized at 1200 °C for 48 hours. b) NbTaTiV homogenized at 1200 °C for 1 week.

Table 2. Measured compositions from Luvak and Anderson Labs. Concentrations are in atomic percent. Characterization techniques are indicated in the second column.

Alloy	Technique	Cr	Fe	Mn	Ni	Nb	Ta	Ti	V	С	N	0	Si	P	S	Cu
Arc-melted Cr ₁₈ Fe ₂₇ Mn ₂₇ Ni ₂₈	IGF, CID, DCPES	17.9	27.6	26.8	27.5	-	-	-	-	0.037	0.039	0.145	0.01	0.009	0.007	0.0016
Arc-melted NbTaTiV	IGF, CID, DCPES	-	-	-	-	24.7	25.3	24.9	25.0	0.131	0.026	0.144	0.0092	< 0.006	< 0.0014	0.0023
VIM Cr ₁₈ Fe ₂₇ Mn ₂₇ Ni ₂₈	IGF, CID, DCPES	17.9	27.5	27.3	26.7	-	-	-	-	0.018	0.428	0.076	0.067	< 0.004	0.014	0.024
VIM NbTaTiV	IGF, CID, DCPES	-	-	-	-	25.6	23.0	24.6	26.2	0.181	< 0.0032	0.091	0.136	0.015	< 0.0014	0.116
VIM Cr ₁₈ Fe ₂₇ Mn ₂₇ Ni ₂₈	ICP-OES	19.0	27.5	25.7	27.4	1 -	-	-	-	0.042	0.016	0.081	0.16	0.02	0.026	0.018
VIM NbTaTiV	ICP-OES	-	-	-	-	25.9	22.4	24.6	26.7	0.098	0.013	0.039	0.03	< 0.015	0.006	0.114

Sections of arc-melted Cr₁₈Fe₂₇Mn₂₇Ni₂₈, arc-melted Cr₁₅Fe₃₅Mn₁₅Ni₃₅, and VIM NbTaTiV were mechanically thinned down to near 100 µm with a mirror finish on both sides and punched into 3-mm disks. V rods were sectioned at an angle such that specimens could fit inside of a 3-mm diameter TEM holder and subsequently thinned to near 100 µm. All specimens as well as the received E90 were electropolished using a Struers TenuPol-5 twin jet electropolisher. Electropolishing parameters used for this work are listed in Table 1.

2.3 Irradiation Experiment

Alloys were irradiated at the IVEM-Tandem facility at ANL, which allows for in situ observation of the microstructural evolution over a wide range of temperatures. The microscope is a Hitachi-9000 TEM operated at 300 keV while the 1 MeV Kr⁺⁺ ion beam is uniform over a 1.5-mm-diameter area [21]. Two irradiation temperatures are used, 50 K and 773 K. E90 and Cr₁₈Fe₂₇Mn₂₇Ni₂₈ were irradiated at cryogenic temperatures (50 K) up to 5 dpa, as estimated by facility-developed correlations between counts measured by a Faraday cup in the microscope and SRIM calculations for the dpa in a 100 nm-thick specimen. Threshold displacement energy was set at 40 eV for all elements in FCC materials, and 60 eV, 90 eV, 30 eV, and 40 eV for Nb, Ta, Ti, and V, respectively [38]. A density of 7.2 g/cm³ was set for the two FCC CSAs, while 7.99 g/cm³, 6.11 g/cm³ and 7.66 g/cm³ were used for E90, V, and NbTaTiV, respectively. The quick KP-calculation was used and the number of displacements was calculated from the sum of cascade energy dissipated by incident ions and recoils to phonons, as outlined in [39]. Atomic % average displacement energies of 40 and 55 eV were used to calculate total displacements for FCC and BCC CSAs, respectively, and the binding energy was set to 0 eV for all elements. Cr₁₈Fe₂₇Mn₂₇Ni₂₈ was also irradiated to 2 dpa at high temperature (773 K). Cr₁₅Fe₃₅Mn₁₅Ni₃₅ was irradiated to 2 dpa at 50 K, 300 K, and 773 K. NbTaTiV and reference materials V and Ni were exclusively irradiated at 50 K. Bright-field and dark-field micrographs were taken by pausing the ion beam at various doses. The imaging conditions used are listed in Table 3. Darkfield micrographs of faulted dislocation loops were taken during in-situ irradiation experiments, and also during post-irradiation examination (PIE) using an FEI Titan Themis 200 scanning transmission electron microscope (STEM), using the relrod contrast condition, housed in the Irradiated Materials Characterization Laboratory (IMCL) at Idaho National Laboratory (INL)

[40]. In some cases, bending of the foils made it difficult to maintain exact imaging conditions between imaging steps. In these cases, micrographs which contain a gradient from a weak to strong condition were obtained. In order to minimize oxidation under the electron beam during high-temperature irradiations, the temperature was raised to 773 K for irradiation but lowered to 573 K for microscopy. Defect densities and size distributions were quantified for each dpa step using ImageJ software to measure loops manually. The size of a cluster or loop was taken as its largest extent in one dimension and the error is the standard deviation. Table 4 shows the matrix of materials and irradiation temperatures while Table 3 lists the fraction of expected defects resolved by each imaging technique. These fractions are calculated by dividing the number of equivalent Burgers' vectors for which g·b is not zero by the total number of equivalent Burgers' vectors. In the case of the g220 contrast condition, defect clusters were assumed to be faulted and their densities were scaled appropriately. Thickness was estimated by thickness fringes in FCC materials where acceptable images were obtained using the strong g200 contrast condition, and otherwise by electron energy-loss spectroscopy (EELS). Electron inelastic mean free paths were estimated by atom-percent-weighted averages of the individual elements. Most error bars on density calculations are a result of uncertainty in these thickness measurements. Thickness calculation from the EELS zero loss peak measures thickness in mean free paths to an accuracy of 10%. For sample thicknesses estimated from thickness fringes, a maximum deviation of 0.5g from the strong g200 condition was assumed. This would result in an approximate 11% overestimation of the extinction distance and thus the thickness, and an equivalent underestimation of the calculated density. This only gives the positive error bar due to the calculation of the effective excitation distance. [41] The negative error bar is estimated as half of the percentage of features which were deemed uncertain while counting.

Table 3. Fractions of which defect types may be resolved with the used contrast conditions based.

Contrast condition	Experiment	% of faulted loops	% of perfect loops		
FCC					
g220	50 K: E90 and Cr ₁₈ Fe ₂₇ Mn ₂₇ Ni ₂₈	50%	83.3%		
g200 near <011>	50 K: Ni and Cr ₁₅ Fe ₃₅ Mn ₁₅ Ni ₃₅ 773 K: Cr ₁₈ Fe ₂₇ Mn ₂₇ Ni ₂₈ and	100%	50%		
Relrod near g311	Cr ₁₅ Fe ₃₅ Mn ₁₅ Ni ₃₅ 50 K: Cr ₁₈ Fe ₂₇ Mn ₂₇ Ni ₂₈ , Cr ₁₅ Fe ₃₅ Mn ₁₅ Ni ₃₅ and E90 300 K: Cr ₁₅ Fe ₃₅ Mn ₁₅ Ni ₃₅	25%	-		
BCC					
g110	50 K: V and NbTaTiV	-	50% of b= a ₀ /2<111> 66.7% of b= a ₀ <100>		

Table 4. Materials, irradiation temperatures, and max dpa of experiments conducted.

Material	50 K	300 K	773 K
Ni	2 dpa	×	×
E90 (FeCr ₁₆ Ni ₁₅)	5 dpa	×	×
$Cr_{18}Fe_{27}Mn_{27}Ni_{28}$	5 dpa	×	2 dpa
$Cr_{15}Fe_{35}Mn_{15}Ni_{35}$	2 dpa	2 dpa	2 dpa
V	2 dpa	×	×
NbTaTiV	2 dpa	×	×

3. Results

3.1 Cryogenic (50 K) Irradiation

3.1.1 Cr₁₈Fe₂₇Mn₂₇Ni₂₈ and E90

The microstructural evolution of the Cr₁₈Fe₂₇Mn₂₇Ni₂₈ and E90 irradiated at 50 K up to 5 dpa is shown in Figure A.1 and Figure A.2. Small dots (black in bright field, white in dark field) begin to appear immediately under irradiation. It is known from literature for FCC and austenitic stainless steels that these features are small defect clusters or precursors of loops [42, 43]. Clusters increase in number with increasing dpa and begin to raft and align into a network [44, 45]. At cryogenic temperature, loops are not expected to grow by the capture of diffusing

defects, but rather defect size increases by this alignment of clusters. This was seen for all cryogenic irradiations of austenitic materials performed, except for pure Ni, and usually results in a slight decrease in defect density as defects begin to merge. Due to the g220 vector used for dark field contrast imaging during these two irradiations, these extended defect structures complicate quantification of defects above 0.3 dpa in Cr₁₈Fe₂₇Mn₂₇Ni₂₈ and 0.5 dpa in E90. Cluster densities and size distributions for this dpa range are included in Figure 3 alongside those of other FCC materials. Since the contrast conditions reveal only a portion of the faulted loops, the cluster densities of Cr₁₈Fe₂₇Mn₂₇Ni₂₈ and E90 were adjusted according to Table 3. Features larger than 16 nm were assumed to be rafts of multiple defect clusters and were not included in size calculations. By 0.3 dpa rafts have an average length of 32±12 nm in Cr₁₈Fe₂₇Mn₂₇Ni₂₈, while individual clusters were more easily distinguished in E90 at 0.5 dpa or below, so no adjustment was made. Diffraction patterns, taken before and after irradiation did not indicate the formation of new phases or significant oxidation on the surfaces of the samples.

Post-irradiation examination (PIE) using relrod contrast revealed faulted dislocation loops of size 17±8 nm in Cr₁₈Fe₂₇Mn₂₇Ni₂₈ and 15±9 nm in E90 after 5 dpa, shown in Figure 4. Whether or not these loops formed under irradiation at 50 K or after subsequently warming the sample back to room temperature for PIE was initially unclear, so relrod contrast imaging was included in subsequent in situ irradiation experiments on Cr₁₅Fe₃₅Mn₁₅Ni₃₅.

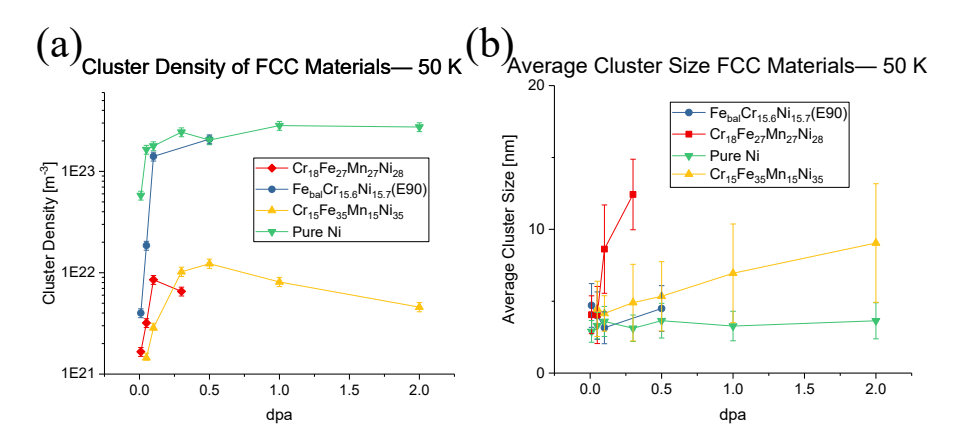


Figure 3. a) Defect density and b) Average loop sizes of FCC materials irradiated at 50 K.

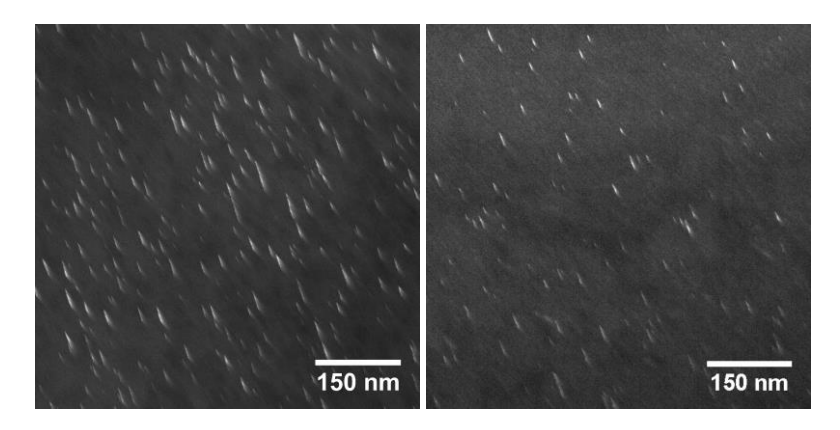


Figure 4. E-90 Model alloy at 50K (imaged at RT), 5 dpa (left) and Cr₁₈Fe₂₇Mn₂₇Ni₂₈ at 50 K (imaged at RT), 5 dpa. (right). Dark field micrographs taken using relrod imaging condition.

$3.1.2 \ Cr_{15}Fe_{35}Mn_{15}Ni_{35}$

Because of the dense network of fringes that formed during 50 K irradiation of Cr₁₈Fe₂₇Mn₂₇Ni₂₈ and E90 above 0.3 and 0.5 dpa, respectively, subsequent samples were irradiated only to 2 dpa to better resolve the microstructural changes. The microstructural evolution of Cr₁₅Fe₃₅Mn₁₅Ni₃₅ is shown in Figure A.3. An increasing density of defect clusters is observed as well as the onset of rafting at 1 and 2 dpa. Diffraction patterns before and after irradiation, not shown here, indicated no formation of new phases or oxidation. Cluster densities and size distributions are shown in Figure 3. The decrease in density is due to the rafting phenomenon which obscures the contrast of smaller clusters. Features larger than 16 nm were assumed to be rafts and no longer individual

defect clusters and were not included in size calculations. By 2 dpa rafts have an average length of 46±33 nm in Cr₁₅Fe₃₅Mn₁₅Ni₃₅.

Faulted loops between 5 and 12 nm long were also resolved while remaining at cryogenic temperatures using the relrod contrast condition at 0.5 dpa and above. Similar loops were resolved in the room temperature irradiation experiment of this material (results not shown here). Example micrographs at 2 dpa are shown in Figure 5. Figure 6 shows the evolution of faulted loop density and size in relation to the dpa. Since the relrod condition reveals one out of four sets of faulted loops, these densities have been scaled to represent the total number of loops. Since faulted loops appear at 50 K and densities are similar between 50 and 300 K in this material, it can be concluded that the faulted loops seen in Figure 4 did in fact form under irradiation and not upon returning the sample back to room temperature. Possibilities for why such loops have been able to form at 50 K while thermal diffusion is suppressed are explored later in the discussion section.

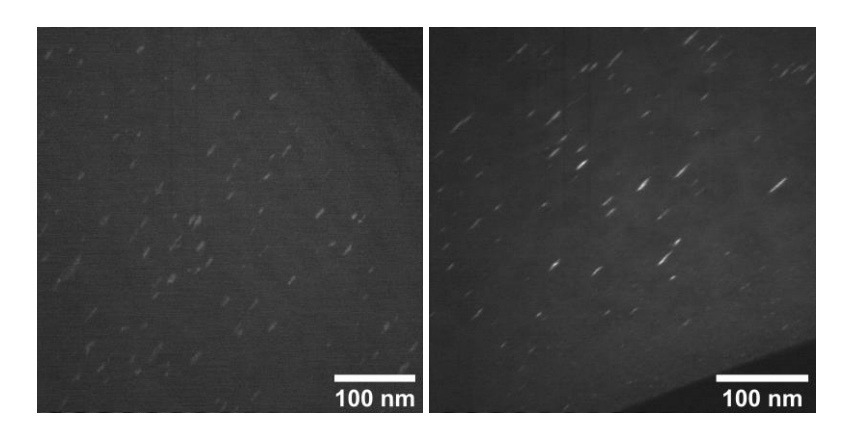


Figure 5. Faulted loops in Cr₁₅Fe₃₅Mn₁₅Ni₃₅ irradiated to 2 dpa at 50 K (left) and 300 K (right). Dark field micrographs taken using relrod imaging condition.

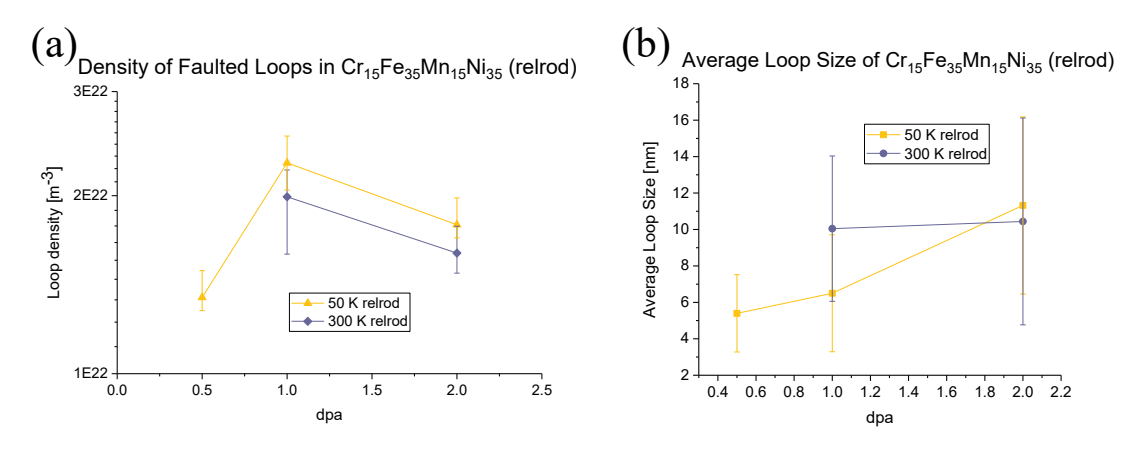


Figure 6. a) Faulted loop density and b) Average loop sizes of Cr₁₅Fe₃₅Mn₁₅Ni₃₅ irradiated at 50 and 300 K.

3.1.3 Pure Ni

The microstructural evolution of pure Ni irradiated to 2 dpa at 50 K is shown in Figure A.4. The cluster densities and size distribution are shown in Figure 3. The density of clusters increases with increasing dpa saturating near 2.7×10^{22} m⁻³. No rafting is observed at 2 dpa, but beyond 1 dpa the specimen begins to bend from the ion beam and defect clusters appear to saturate and be most visible where the sample bends toward a slightly stronger imaging condition. Compared to the two FCC CSA compositions, pure Ni and model alloy E90 both had a higher density of defects at each dpa step as well as less growth of clusters. Rafting behavior did occur in E90 above 0.5 dpa. Diffraction patterns of the <011> zone axis before and after irradiation revealed the appearance polycrystalline rings which likely correspond to some oxidation on the surface of the Ni sample during irradiation.

3.1.4 NbTaTiV and Pure V

Figure A.5 and Figure A.6 show the microstructural evolutions of NbTaTiV and the pure V, irradiated to 2 dpa at 50 K, respectively. After the first irradiation step to 0.01 dpa, defects could

only be seen found in NbTaTiV in the area shown, but at later steps better contrast was found slightly farther from the edge of the electron transparent area. The thin area of the pure V showed a complex network of fringes due to the rough surface created by electropolishing, but this contrast is eventually weak compared to that of radiation-induced defects. Diffraction patterns before and after irradiation showed no evidence of oxidation. As with the FCC materials under irradiation, black dots appear in the bright field and white dots in the dark field. However, because of the intrinsically high stacking-fault energy of BCC materials, these clusters nucleate ideal loops with Burgers vectors of $a_0/2 < 111 > or a_0 < 100 > if they reach a critical size rather than$ faulted loops which nucleate in FCC materials. Dislocations with both these Burgers vectors may be resolved by the g110 contrast condition, which was used here to resolve small defect clusters which exert a strain field in the relevant planes. Cluster densities and average cluster size are shown in Figure 7. The number of clusters appears to saturate in both materials, with the density in pure V approximately three times that of equimolar NbTaTiV. Despite this difference in density the average size of clusters is approximately similar in NbTaTiV. The average cluster sizes in both materials also do not change significantly or deviate from one another with increasing dpa.

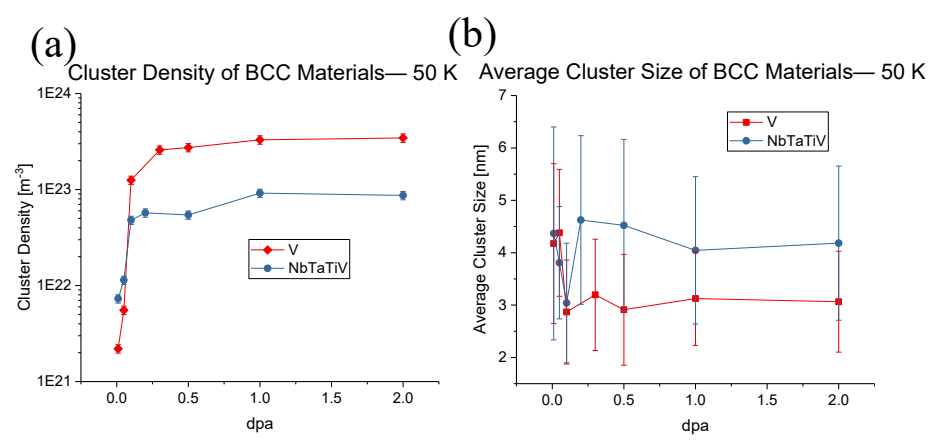


Figure 7. a) Defect cluster density and b) Average cluster sizes of NbTaTiV and pure V irradiated at 50 K.

3.2 High-Temperature (773 K) Irradiation of Cr₁₅Fe₃₅Mn₁₅Ni₃₅ and Cr₁₈Fe₂₇Mn₂₇Ni₂₈

The microstructural evolutions of the two FCC CSA compositions irradiated at 773 K to 2 dpa are shown in Figure A.7 and Figure A.8. These densities are calculated using only the average thickness in the region quantified, so the density may be underestimated. Small interstitial clusters form at first but eventually evolve into loops which grow by absorption of additional interstitial defects [43, 46]. Between 1 and 2 dpa of damage, edge-on loops became observable in both materials which indicates that these are indeed faulted loops because at this zone, two sets of 1/3<111> type loops will be edge on. Diffraction patterns before and after irradiation showed some minor oxidation in both alloys. Loop density is higher in Cr₁₅Fe₃₅Mn₁₅Ni₃₅ than Cr₁₈Fe₂₇Mn₂₇Ni₂₈ while average loop size follows the opposite trend. Higher magnification images at 2 dpa show this size difference in Figure 8. Loop densities and average loop sizes for both alloys are shown in Figure 9, while box-and-whisker plots showing the loop size distributions are shown in Figure 10. Loops grow generally twice as quickly in Cr₁₈Fe₂₇Mn₂₇Ni₂₈ than in Cr₁₅Fe₃₅Mn₁₅Ni₃₅, though both maintain the same distribution shape.

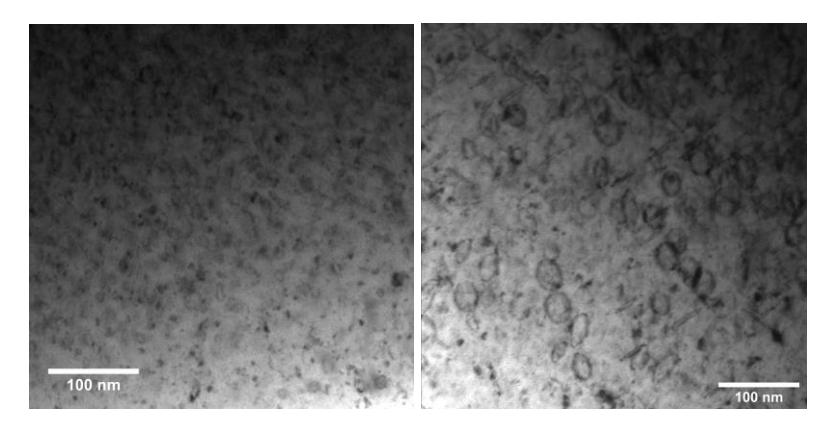


Figure 8. Bright field images taken near <011> zone axis showing size difference between loops in Cr₁₅Fe₃₅Mn₁₅Ni₃₅ (left) and Cr₁₈Fe₂₇Mn₂₇Ni₂₈ (right) at 2 dpa.

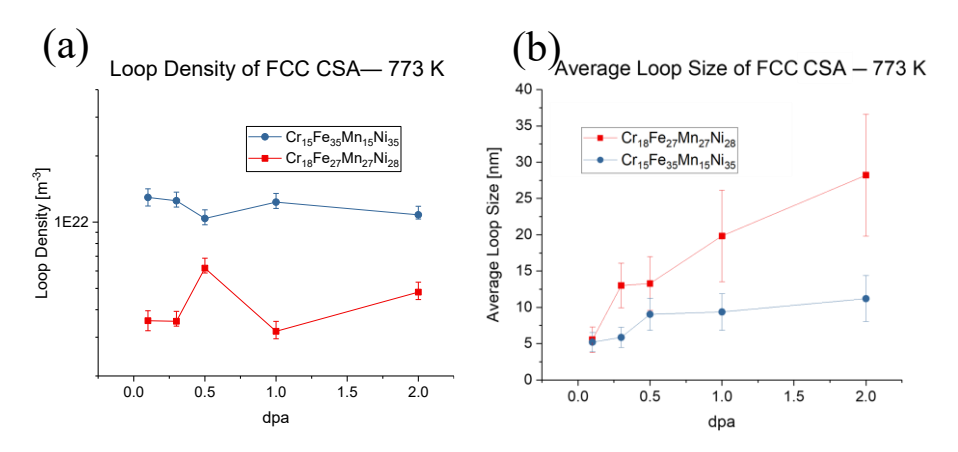


Figure 9. a) Faulted loop density and b) Average loop sizes of Cr₁₈Fe₂₇Mn₂₇Ni₂₈ and Cr₁₅Fe₃₅Mn₁₅Ni₃₅ irradiated at 773 K.

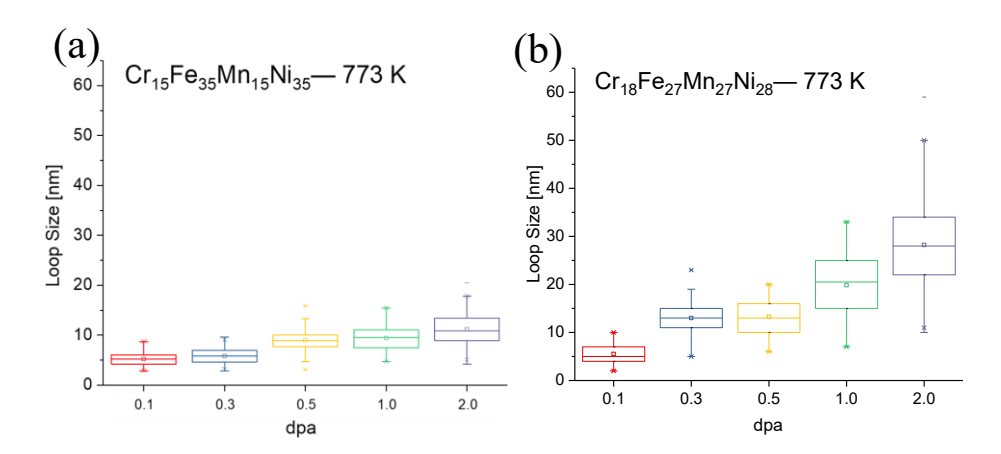


Figure 10. Loop size distributions for a) Cr₁₅Fe₃₅Mn₁₅Ni₃₅ and b) Cr₁₈Fe₂₇Mn₂₇Ni₂₈ irradiated at 773 K.

4. Discussion

4.1 Cryogenic Irradiation Experiment

Although void swelling is the principle radiation damage concern for nuclear structural materials for fast reactors, no materials exhibited voids in this study. This is likely due to the irradiation conditions (low temperature, low dpa, and lack of stabilizing gas), as void swelling usually has an incubation period in the tens of dpas. [47] The primary form of damage accumulation in cryogenic irradiations is by small vacancy and interstitial defect clusters, which also form during irradiation at higher temperature but can grow and form loops due to more favorable thermal

diffusion kinetics. At cryogenic temperatures, defect clusters become resolvable by TEM after they grow large enough to disturb the stress field and be visible under TEM, which is usually assisted by the overlapping of cascades. Although these clusters have not yet collapsed into loops, they are assumed to provide the best diffraction contrast under the same imaging conditions as the loops which commonly form based in the compact planes of the material as shown in Table 3. It was shown in vacancy loop nucleation in aluminum that vacancy clusters which have yet to grow to a critical size and collapse into loops more closely resemble a bloated disk of vacancies than a perfect sphere [48]. It follows that the plane of this disk is along the plane most favorable for loop formation for both vacancies and interstitials. These defects do not grow significantly larger by thermal diffusion of additional defects but instead experience beamassisted or athermal stress-induced 1D diffusion which causes them to align into the rafts shown in Figure A.1 and Figure A.2. Dislocation rafts are a typical feature in cryogenic irradiations that are substantially below the temperature threshold for thermally activated diffusion [49]. The influence of this mobility is supported by the confirmation that edge-on faulted loops, resolved by relrod contrast, form under irradiation, even at 50 K. These loops were only found above 0.5 dpa for the cryogenic irradiation when the relrod streak became visible in the diffraction pattern and could be selected for a dark field condition. By that dpa level, the contrast of the rafting and other defects obscured such loops in the simpler imaging conditions. By this point the rafting of clusters obscures the contrast of even the weak 2-beam condition such that these loops are not resolvable except by relrod contrast. The source of mobility for the individual point defects or clusters to reach these loops at 50 K needs further investigation. Comparing the FCC and BCC materials directly, the cluster density in NbTaTiV was higher than that of the FCC CSAs and yet lower than the less complex FCC materials. The clusters seen in BCC materials also remain

smaller than 10 nm and do not experience rafting by 2 dpa, suggesting that their mobility is reduced by the larger atomic size and mass fluctuations in light refractory compared to austenitic CSAs.

At 50 K it is assumed that that diffusion of point defects to sinks is negligible such that the density of these clusters provides a direct measure of point defect production. Both FCC CSA compositions exhibited slower accumulation of defect clusters with increasing dpa compared to E90 or pure Ni, saturating at a density approximately an order of magnitude lower than either of the less compositionally complex systems $(1x10^{22} \text{ m}^{-3} \text{ vs. } 1x10^{23} \text{ m}^{-3})$. The measured density in E90 is consistent with previous irradiations performed on E90 at 300 °C [50]. The results also align with recent work which used Rutherford backscatter spectrometry along a channeling direction (RBS/C) and Monte Carlo (MC) simulations to confirm a lower concentration of defects in NiFeCoCr and NiFe compared to pure Ni during 500 keV Ar⁺ irradiation at 16 K. [51] The average cluster sizes followed the opposite trend of cluster density. Comparing Cr₁₅Fe₃₅Mn₁₅Ni₃₅ to Cr₁₈Fe₂₇Mn₂₇Ni₂₈, the average cluster size is smaller but the densities are similar. This may be a result of the different g-vectors used in these experiments, or it may indicate some compositional dependence of the defect production term. NbTaTiV also showed reduced defect production compared to pure V, saturating at $\sim 1/3$ of the cluster density of pure V. These results support one hypothesis for CSA radiation resistance, which attributes a reduction in defect production in CSA to heat transport modes during the thermal spike. It has been proposed that the lattice distortion effect as well as atomic mass, size, and force constant fluctuations between lattice sites in CSAs cause significant scattering of phonons and electrons compared to less compositionally complex materials, decreasing the mean-free path of heat transported away from the displacement cascade [26-31, 52-57]. Beland et al. showed that

electron thermal conductivities are reduced in HEA and that a reduction in thermal conductivity by a factor α would imply an increase in quenching time by a factor $1/\alpha$ [58]. The resulting increase in quenching time is assumed to allow for more recombination of point defects before recrystallization, although it was also shown by simulation that the reduction of surviving point defects was small in NiFe compared to Ni [30]. The results presented here suggest that CSAs may show fewer surviving point defects post cascade quench, implying slower point defect production. If this is the case, the threshold dose for defect clusters to saturate should be higher for CSAs in Figure 3 and Figure 7, but roughly similar saturation doses are observed. Perhaps the densities appear to saturate as they raft together and density decreases. The theory also implies that CSAs with larger variations in atomic size and mass should have the greatest reduction in point defect production, but this is not the case for this work, as the reduction in defect cluster density in the BCC CSAs was less pronounced than in their FCC counterparts despite similar densities in the simpler materials. It is also noted, that the above theory contradicts a longstanding theory about displacement cascade evolution, which assumes that energetic interstitial atoms, ejected to the periphery of the displacement cascade by replacement collision sequences, can exit the region affected by the thermal spike, leaving the molten core of the displacement cascade with a lower atomic density. As the recrystallized solid front advances inward, atoms initially fill every lattice site and no vacancies are frozen in. The temperature gradient and the recrystallization effect result in a naturally lower density of the displacement cascade core, as vacancies are forced to cluster at the center. Slower cooling allows more time for density fluctuations to affect the migration of vacancies to the core, increasing the spatial separation of vacancies and interstitials and slowing their intra-cascade recombination. Enhanced vacancy clustering within the cascade core would then lead to a higher density of stacking-fault

tetrahedra, whereas a comparably quick cooling time would leave point defects more evenly dispersed throughout the cascade volume [59].

4.2 High Temperature Irradiation Experiment

Other theories to explain the mechanism of improved radiation resistance of CSAs focus on individual defect and cluster migration after the displacement cascade has cooled and are largely derived from the lattice distortion and sluggish diffusion hypotheses. Sluggish diffusion is believed to slow the agglomeration of point defects into clusters and larger extended defects. However, sluggish diffusion has been found to be highly alloy dependent due to differences in diffusion parameters and their temperature dependence. Sluggish diffusion and radiation resistance are therefore not simply functions of the number of alloying elements [60, 61]. Lattice distortion was shown to inhibit the long range 1D motion of glissile interstitial clusters and loops which would typically annihilate at sinks. In CSAs, glide of small interstitial clusters is rather defocused into 3D motion because random lattice distortions, more prominent in CSAs, may reorient the glide cylinder [19]. As a result, interstitial loops may remain more localized in CSAs and absorb more vacancies, resulting in less localized vacancy super-saturation thereby inhibiting void nucleation. This increased absorption of vacancies would reduce void nucleation, but not necessarily cause a significant reduction in interstitial loop growth. These results do not support the swelling resistance of CSAs but do support the notion that compositional changes can have a large influence on the formation of interstitial loops and likely of other extended defects. It has also been suggested that rather than all species experiencing slower diffusion, the gap in migration energy between interstitial atoms and vacancies is decreased by lattice distortion [62]. That is, vacancies become more mobile while interstitials become less mobile

[18]. This is thought to facilitate short-range recombination of irradiation induced point defects, allowing the recombination regime of defect evolution to occur after less defect accumulation. Thus, at higher temperatures, it is expected that increased compositional complexity results in suppressed point defect production during the displacement cascade and, for a given dose rate, favors an earlier recombination regime. Reduced mobility of larger defect structures, such as clusters and loops, slows the formation of point defect super-saturations, such as that of vacancies, which is a prerequisite for void swelling.

At 773 K, interstitial dislocation loops begin as the small clusters observed at 50 K but can grow by thermal diffusion of radiation-induced interstitials. Clusters grow by capturing more interstitials than vacancies until they reach a critical size and collapse to form a faulted loop. The difference in microstructural evolution between cryogenic temperature and high temperature is illustrated in Figure 11. Compared to in situ irradiation of other CSAs at 773K, the average size of loops in Cr₁₈Fe₂₇Mn₂₇Ni₂₈ is consistent with the 20-25 nm loop size observed in two other FCC SP-CSAs, Al_{0.3}CoCrFeNi and CoCrFeMnNi. On the other hand, loops in Cr₁₅Fe₃₅Mn₁₅Ni₃₅ are slightly smaller than the 14 nm average loop size observed in pure Ni at similar dpas [63]. As can be seen in Figure 12, the results are consistent with other CSAs irradiated under the same conditions. The loop densities and average sizes are comparable to the more complex SP-CSAs, except for the nearly twice as large average size of loops in Cr₁₈Fe₂₇Mn₂₇Ni₂₈ [46]. Modeling studies suggest that compositional complexity and the consideration of phonon-electron coupling results in a lower density of smaller defect clusters, which seemingly contradicts the larger loops that were observed by Shi as well as this work [64]. However, such simulations only model the direct result of the displacement cascade. Interstitial defect clusters must acquire more atoms by migration and/or overlap with other clusters in order to nucleate loops, and if their production is

reduced, fewer loops are able to nucleate before they begin to grow. If loops begin to grow with similar or only slightly reduced defect production, they will grow larger in alloys which have nucleated fewer loops. The observed difference in interstitial loop growth rates between the two FCC CSAs demonstrates the large effect that composition may have on defect mobility and microstructural evolution under irradiation within a CSA family. The thickness of each irradiated foil was comparable, estimated by thickness of fringes to be 120 nm and 140 nm for Cr₁₈Fe₂₇Mn₂₇Ni₂₈ and Cr₁₅Fe₃₅Mn₁₅Ni₃₅, respectively, which rules out the possibility of the sink effect from the foil surfaces compounding the results. The difference in loop growth kinetics is attributed to the only element which differs significantly between the two compositions, namely Mn. Mn may affect the nucleation rate of interstitial loops by its effect on (i) vacancy mobility and/or (ii) stacking-fault energy (SFE) of the matrix. Regarding (i), although Mn is the fastest diffuser in the CoCrFeMnNi system, it was also found that sluggish diffusion of individual atoms on a T_m-relative temperature scale is only present in Mn-containing alloys from said system [60]. The lower concentration of Mn in Cr₁₅Fe₃₅Mn₁₅Ni₃₅ may reduce the overall mobility of vacancies, which diffuse by switching places with matrix atoms. Lower Mn content means vacancies diffuse by switching with fewer of these more mobile atoms. This would reduce the arrival rate of vacancies to interstitial clusters, effectively increasing the nucleation rate of faulted interstitial loops [65]. As mentioned above, once loops begin to grow, similar levels of irradiation induced point defects are spread across more loops, such that this higher density of loops would grow more slowly compared to a higher Mn-containing alloy. Regarding the second mechanism (ii), it is noted that the nucleation of a loop in an FCC material requires the collapse of a cluster into a faulted loop. The SFE contributes to the energy barrier for cluster collapse. Tailoring of the strength, ductility, and strain-hardening behavior of high Mn F-M steels has long focused on the influence of SFE through transformation- and twinning-induced plasticity (TRIP and TWIP) mechanisms [66]. It has been shown that addition of Mn in austenitic stainless steels reduces the SFE to a minimum near 15 wt% Mn at 300 K, after which further Mn addition begins to increase the SFE [67]. It has also been shown that CSAs experience higher local fluctuations in SFE compared to less compositionally complex alloys. This is a result of the large variation and tunability of the SFE with local chemical composition and short-range order, which would reduce point defect production and increase the onset stress for dislocation movement [68, 69]. Under typical applied stresses, these fluctuations hinder the mobility of loops that may encounter new energy barriers along their glide cylinders and find it energetically favorable to reorient. As loops grow larger, they may also unfault and become network dislocations with higher probability if the Shockley partial sweeps through a region with a large local increase in SFE. Direct measurement of the SFEs of FCC CSA systems and determination of the effect of Mn content on those SFEs would be necessary to further confirm that these mechanisms are at play in irradiation-induced loop growth. High-throughput experimentation and computational techniques may supplement these efforts by efficiently probing the composition space for favorable attributes such as SFE or degree of SFE fluctuations.

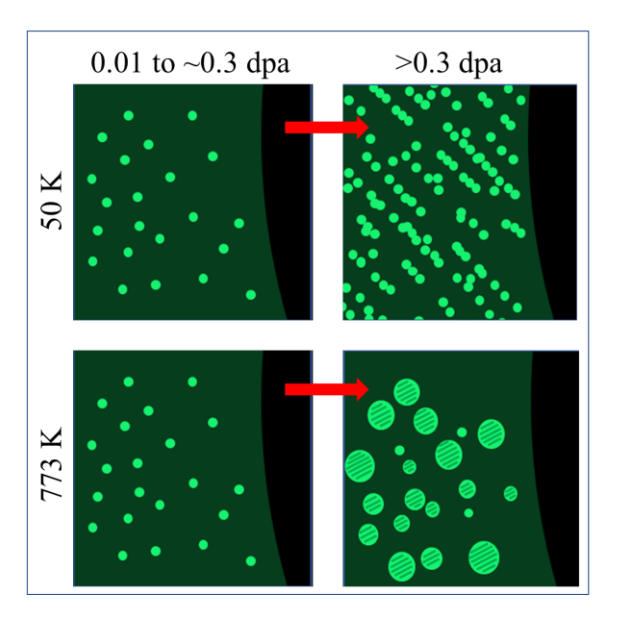


Figure 11. Comparison of the microstructural evolution in CSAs at 50 K and 773 K. Initially small clusters form in at both temperatures, but clusters raft at low temperature while interstitial loops are able to grow at high temperature.

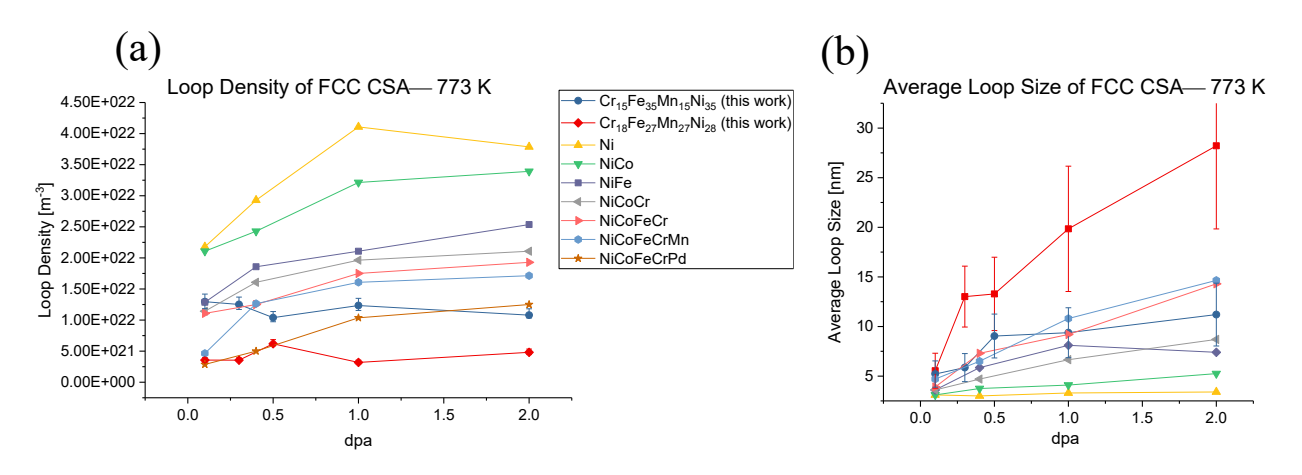


Figure 12. a) Loop density and b) Average size evolutions of various SP-CSA irradiated to 2 dpa at 773 K by Shi *et al.* compared to those of Cr₁₈Fe₂₇Mn₂₇Ni₂₈ and Cr₁₅Fe₃₅Mn₁₅Ni₃₅ [41].

5. Conclusions

Three complex concentrated alloys, Cr₁₈Fe₂₇Mn₂₇Ni₂₈, Cr₁₅Fe₃₅Mn₁₅Ni₃₅, and NbTaTiV, along with reference materials (pure Ni and E90 for the CrFeMnNi family and pure V for NbTaTiV) were irradiated at 50 K and 773 K with 1 MeV Kr ions to various dpa using in situ TEM

techniques. The cryogenic irradiations resulted in a high density of small defect clusters and a lower density of faulted dislocation loops as large as 12 nm in the FCC CSAs, implying that individual point defects are not entirely immobile at under these conditions. The small defect clusters undergo rafting to form a network of parallel fringes nearing the point of saturation. With diffusion still strongly suppressed, defect densities were lower in both FCC and BCC CSAs than in their less compositionally complex reference materials which supports the theory that point defect production during the displacement cascade is reduced in CSAs. However, because the FCC CSAs showed a greater reduction in defect cluster density, the notion that larger variation in atomic size and mass causes a greater reduction in point defect production is not supported. Slower defect production implies a slower overall evolution of defect loops to vacancy super-saturation and void swelling. High-temperature irradiations of the two FCC CSAs resulted in the formation of interstitial dislocation loops which grow with increasing dpa to an average size of 27 nm in Cr₁₈Fe₂₇Mn₂₇Ni₂₈ and 10 nm in Cr₁₅Fe₃₅Mn₁₅Ni₃₅. This difference in loop growth kinetics was attributed to the difference in Mn-content due to its effect on the nucleation rate by increasing vacancy mobility and/or the SFE minimum near 15 wt% Mn. The results of this work demonstrate the influence of composition on faulted loop nucleation and the evolution of microstructure under irradiation. The SFE may be a useful parameter for determining the irradiation resistance of austenitic CSAs as well as their strength, ductility, and strain-hardening behavior. Future work should focus on experimental verification of differences in SFE in FCC CSAs, as well as high temperature in situ irradiation experiments with He coimplantation to promote the formation of voids. This result also underscores the necessity for high-throughput mapping of radiation effects by combining novel manufacturing techniques such as magnetron-sputtered combinatorial thin-film synthesis and laser metal deposition 3D printing with complimentary high-throughput irradiation and characterization techniques.

6. Acknowledgements

This research is being performed using funding received from the DOE Office of Nuclear Energy's Nuclear Energy University Program (project ID #17-12463). This material is based upon work supported under an Integrated University Program Graduate Fellowship.

The authors gratefully acknowledge use of facilities and instrumentation at the UW-Madison Wisconsin Centers for Nanoscale Technology (wcnt.wisc.edu) partially supported by the NSF through the University of Wisconsin Materials Research Science and Engineering Center (DMR-1720415).

Arc-melting work using the Arcast Arc200 was made possible by Professor Dan Thoma, who manages the Alloy Design and De-velopment Laboratory at the University of Wisconsin-Madison.

The irradiation experiments were carried out over the course of two rapid turnaround experiments, (proposal ID #17-1118 and #18-1610) using funding provided by the Nuclear Science User Facilities.

This work was performed, in part, at the Irradiated Materials Characterization Laboratory at Idaho National Laboratory as part of a rapid turnaround experiment (proposal ID #18-1380) using funding provided by Nuclear Science User Facilities.

This work was performed, in part, at the Center for Nanoscale Materials, a U.S. Department of Energy Office of Science User Facility, and supported by the U.S. Department of Energy, Office of Science, under Contract No. DE-AC02-06CH11357.

The author would also like to acknowledge the IVEM staff Pete Baldo and Ed Ryan for their advice and technical assistance, as well as Dr. Frank Garner for expert guidance and supply of model alloy E90.

7. References

- [1] T.R. Allen, D. Kaoumi, J.P. Wharry, Z. Jiao, C. Topbasi, A. Kohnert, L. Barnard, A. Certain, K.G. Field, G.S. Was, D.L. Morgan, A.T. Motta, B.D. Wirth, Y. Yang, Characterization of microstructure and property evolution in advanced cladding and duct: Materials exposed to high dose and elevated temperature, Journal of Materials Research 30(09) (2015) 1246-1274.
- [2] G.V. Prasad Reddy, R. Sandhya, K. Laha, Advanced Materials for Indian Future Nuclear Energy Systems, in: K.V. Raghavan, P. Ghosh (Eds.), Energy Engineering: Proceedings of CAETS 2015 Convocation on Pathways to Sustainability, Springer Singapore, Singapore, 2017, pp. 179-181.
- [3] M.B. Toloczko, F.A. Garner, C.R. Eiholzer, Irradiation creep and swelling of the US fusion heats of HT9 and 9Cr-1Mo to 208 dpa at $\sim 400^{\circ}$ C, Journal of Nuclear Materials 212 (1994) 604-607.
- [4] Y.J. Zhou, Y. Zhang, Y.L. Wang, G.L. Chen, Solid solution alloys of AlCoCrFeNiTix with excellent room-temperature mechanical properties, Applied Physics Letters 90(18) (2007) 181904.
- [5] P. Yvon, M. Le Flem, C. Cabet, J.L. Seran, Structural materials for next generation nuclear systems: Challenges and the path forward, Nuclear Engineering and Design 294 (2015) 161-169.
- [6] K. Jin, H. Bei, Single-Phase Concentrated Solid-Solution Alloys: Bridging Intrinsic Transport Properties and Irradiation Resistance, Frontiers in Materials 5(26) (2018).
- [7] D. Miracle, O. Senkov, A critical review of high entropy alloys and related concepts, Acta Materialia 122 (2017) 448 511.
- [8] J.W. Yeh, S.K. Chen, S.J. Lin, J.Y. Gan, T.S. Chin, T.T. Shun, C.H. Tsau, S.Y. Chang, Nanostructured High-Entropy Alloys with Multiple Principal Elements: Novel Alloy Design Concepts and Outcomes, Advanced Engineering Materials 6(5) (2004) 299-303.
- [9] S. Gorsse, D.B. Miracle, O.N. Senkov, Mapping the world of complex concentrated alloys, Acta Materialia 135(177-187) (2017).
- [10] Z. Fan, T. Yang, B. Kombaiah, X. Wang, P.D. Edmondson, Y.N. Osetsky, K. Jin, C. Lu, H. Bei, L. Wang, K.L. More, W.J. Weber, Y. Zhang, From suppressed void growth to significant void swelling in NiCoFeCr complex concentrated solid-solution alloy, Materialia 9 (2020).
- [11] F.X. Zhang, S. Zhao, K. Jin, H. Xue, G. Velisa, H. Bei, R. Huang, J.Y.P. Ko, D.C. Pagan, J.C. Neuefeind, W.J. Weber, Y. Zhang, Local Structure and Short-Range Order in a NiCoCr Solid Solution Alloy, Physical Review Letters 118 (2017).
- [12] A. Tamm, A. Aabloo, M. Klintenberg, M. Stocks, A. Caro, Atomic-scale properties of Ni-based FCC ternary, and quaternary alloys, Acta Materialia 99 (2015) 307-312.

- [13] C. Niu, A.J. Zaddach, A.A. Oni, X. Sang, J.W. Hurt III, J.M. LeBeau, C.C. Koch, D.L. Irving, Spindriven ordering of Cr in the equiatomic high entropy alloy NiFeCrCo, Applied Physics Letters 106 (2015).
- [14] N.A.P.K. Kumar, C. Li, K.J. Leonard, H. Bei, S.J. Zinkle, Microstructural stability and mechanical behavior of FeNiMnCr high entropy alloy under ion irradiation, Acta Materialia 113 (2016) 230-244.
- [15] N. Jia, Y. Li, X. Liu, Y. Zheng, B. Wang, J. Wang, Y. Xue, K. Jin, Thermal Stability and Mechanical Properties of Low-Activation Single-Phase Ti-V-Ta Medium Entropy Alloys, JOM (2019) 1-9.
- [16] T. Egami, W. Guo, P.D. Rack, T. Nagase, Irradiation Resistance of Multicomponent Alloys, Metallurgical and Materials Transactions A 45 (2013) 180-183.
- [17] K. Jin, C. Lu, L.M. Wang, J. Qu, W.J. Weber, Y. Zhang, H. Bei, Effects of compositional complexity on the ion-irradiation induced swelling and hardening in Ni-containing equiatomic alloys, Scripta Materialia 119 (2016) 65-70.
- [18] T. Yang, C. Li, S.J. Zinkle, S. Zhao, H. Bei, Y. Zhang, Irradiation responses and defect behavior of single-phase concentrated solid solution alloys, Journal of Materials Research 33(19) (2018) 3077-3091.
- [19] C. Lu, L. Niu, N. Chen, K. Jin, T. Yang, P. Xiu, Y. Zhang, F. Gao, H. Bei, S. Shi, M.-R. He, I.M. Robertson, W.J. Weber, L. Wang, Enhancing radiation tolerance by controlling defect mobility and migration pathways in multicomponent single-phase alloys, Nature Communications 7 (2016) 13564.
- [20] C. Lu, T. Yang, K. Jin, N. Gao, P. Xiu, Y. Zhang, F. Gao, H. Bei, W.J. Weber, K. Sun, Y. Dong, L. Wang, Radiation-induced segregation on defect clusters in single-phase concentrated solid-solution alloys, Acta Materialia 127 (2017) 98-107.
- [21] W.-Y. Chen, X. Liu, Y. Chen, J.-W. Yeh, K.-K. Tseng, K. Natesan, Irradiation effects in high entropy alloys and 316H stainless steel at 300 °C, Journal of Nuclear Materials 510 (2018) 421-430.
- [22] C. Li, X. Hu, T. Yang, K.K. N.A.P., B.D. Wirth, S.J. Zinkle, Neutron irradiation response of a Cofree high entropy alloy, Journal of Nuclear Materials Neutron irradiation response of a Cofree high entropy alloy (2019).
- [23] G.S. Was, D. Petti, S. Ukai, S. Zinkle, Materials for Future Nuclear Energy Systems, Journal of Nuclear Materials (2019).
- [24] C. Topbasi, D. Kaoumi, A. Motta, M. Kirk, Microstructural evolution in NF616 (P92) and Fe–9Cr–0.1C-model alloy under heavy ion irradiation, Journal of Nuclear Materials 466 (2015) 179 186.
- [25] T. Egami, M. Ojha, O. Khorgolkhuu, D.M. Nicholson, G.M. Stocks, Local Electronic Effects and Irradiation Resistance in High-Entropy Alloys, The Journal of The Minerals, Metals & Materials Society 67(10) (2015) 2345 2349.
- [26] F. Körmann, Y. Ikeda, B. Grabowski, M. Sluiter, Phonon broadening in high entropy alloys, Computational Materials Science 3 (2017).
- [27] Y. Zhang, K. Jin, H. Xue, C. Lu, R.J. Olsen, L.K. Beland, M.W. Ullah, S. Zhao, H. Bei, D.S. Aidhy,
- G.D. Samolyuk, L. Wang, M. Caro, A. Caro, G.M. Stocks, B.C. Larson, I.M. Robertson, A.A. Correa,
- W.J. Weber, Influence of chemical disorder on energy dissipation and defect evolution in advanced alloys, Journal of Materials Research 31(16) (2016) 2363-2375.
- [28] S. Zhao, Y. Osetsky, A.V. Barashev, Y. Zhang, Frenkel defect recombination in Ni and Nicontaining concentrated solid-solution alloys, Acta Materialia 173 (2019) 184-194.
- [29] M. Caro, L.K. Béland, G.D. Samolyuk, R.E. Stoller, A. Caro, Lattice thermal conductivity of multi-component alloys, Journal of Alloys and Compounds 648 (2015) 408-413.
- [30] L. Béland, Y. Osetsky, R. Stoller, The effect of alloying nickel with iron on the supersonic ballistic stage of high energy displacement cascades, Acta Materialia 116 (2016) 136 142.
- [31] Y. Zhang, G. Stocks, K. Jin, C. Lu, H. Bei, B. Sales, L. Wang, L. Béland, R. Stoller, G. Samolyuk, M. Caro, A. Caro, W.J. Weber, Influence of chemical disorder on energy dissipation and defect evolution in concentrated solid solution alloys, Nature Communications 6 (2015).
- [32] B. Cantor, I.T.H. Chang, P. Knight, A.J.B. Vincent, Microstructural development in equiatomic multicomponent alloys, Materials Science and Engineering: A 375 377 (2004) 213 218.

- [33] M. Elbakhshwan, W. Doniger, C. Falconer, M. Moorehead, C. Parkin, C. Zhang, K. Sridharan, A. Couet, Corrosion and Thermal Stability of CrMnFeNi High Entropy Alloy in Molten FLiBe Salt, Scientific Reports 9(1) (2019) 18993.
- [34] S. Ohnuki, F.A. Garner, H. Takahashi, Phase Instability and Void Formation in Neutron-Irradiated Fe-Cr-Mn-Ni Alloys, Materials Transactions 34 (1993).
- [35] C. Sun, L. Malerba, M.J. Konstantinovic, F.A. Garner, S.A. Maloy, Emulating Neutron-Induced Void Swelling in Stainless Steels Using Ion Irradiation, Proceedings of the 18th International Conference on Environmental Degradation of Materials in Nuclear Power Systems Water Reactors (2018).
- [36] F.A. Garner, M.B. Toloczko, B.H. Sencer, Comparison of swelling and irradiation creep behavior of fcc-austenitic and bcc-ferritic/martensitic alloys at high neutron exposure, Journal of Nuclear Materials 276(1–3) (2000) 123-142.
- [37] D.J.M. King, S.T.Y. Cheung, S.A. Humphry-Baker, C. Parkin, A. Couet, M.B. Cortie, G.R. Lumpkin, S.C. Middleburgh, A.J. Knowles, High temperature, low neutron cross-section high-entropy alloys in the Nb-Ti-V-Zr system, Acta Materialia 166 (2019) 435-446.
- [38] ASTM, Standard Practice for Investigating the Effects of Neutron Radiation Damage Using Charged-Particle Irradiation, 2018.
- [39] R.E. Stoller, M.B. Toloczko, G.S. Was, A.G. Certain, S. Dwaraknath, F.A. Garner, On the use of SRIM for computing radiation damage exposure, Nuclear Instruments and Methods in Physics Research Section B: Beam Interactions with Materials and Atoms 310 (2013) 75-80.
- [40] Y. Yang, Y. Chen, Y. Huang, T. Allen, A. Rao, Irradiation Microstructure of Austenitic Steels and Cast Steels Irradiated in the BOR-60 Reactor at 320°C, Proceedings of the 15th International Conference on Environmental Degradation of Materials in Nuclear Power Systems Water Reactors (2011) 2137-2149.
- [41] D.B. Williams, C.B. Carter, Transmission Electron Microscopy, A Textbook for Materials Science, Springer (2009).
- [42] M.R. He, S. Wang, K. Jin, H. Bei, K. Yasuda, S. Matsumura, K. Higashida, I. Robertson, Enhanced damage resistance and novel defect structure of CrFeCoNi under in situ electron irradiation, Scripta Materialia 125 (2016) 5 9.
- [43] S.J. Zinkle, P.J. Maziasz, R.E. Stoller, Dose dependence of the microstructural evolution in neutron-irradiated austenitic stainless steel, Journal of Nuclear Materials 206(2-3) (1993) 266-286.
- [44] D. Kaoumi, J. Adamson, Self-ordered defect structures in two model F/M steels under in situ ion irradiation, Journal of Nuclear Materials 448(1 3) (2014) 233 238.
- [45] C. Xu, W.Y. Chen, Y. Chen, Y. Yang, Microstructural evolution of NF709 austenitic stainless steel under in situ ion irradiations at room temperature, 300, 400, 500 and 600 C, Journal of Nuclear Materials 509 (2018) 644-653.
- [46] S. Shi, M.R. He, K. Jin, H. Bei, I.M. Robertson, Evolution of ion damage at 773K in Ni- containing concentrated solid-solution alloys, Journal of Nuclear Materials 501 (2018) 132-142.
- [47] F.A. Garner, C.A. Black, D.J. Edwards, Factors which control the swelling of Fe-Cr-Ni ternary austenitic alloys, Journal of Nuclear Materials 245(2 3) (1997) 124 130.
- [48] T.L. Davis, Nucleation Rate of Vacancy Clusters in Aluminum, Journal of Applied Physics 38(9) (1967) 3756-3760.
- [49] M. Kirk, M. Li, D. Xu, B.D. Wirth, Predicting neutron damage using TEM with in situ ion irradiation and computer modeling, Journal of Nuclear Materials 498 (2018) 199-212.
- [50] T. Okita, N. Sekimura, T. Iwai, F.A. Garner, Investigation of The Synergistic Influence of Irradiation Temperature and Atomic Displacement Rate on the Microstructural Evolution of Ion-Irradiated Model Austenitic Alloy Fe-15Cr-16Ni, 10th International Conference on Environmental Degradation of Materials in Nuclear Power Systems, Lake Tahoe NV, 2001.
- [51] C. Mieszczynski, R. Ratajczak, J. Jagielski, G. Velişa, H. Bei, B.C. Sales, E. Wendler, W.J. Weber, Y. Zhang, Defect evolution in Ni and solid-solution alloys of NiFe and NiFeCoCr under ion irradiation at 16 and 300 K, Journal of Nuclear Materials (2020).

- [52] M.S. Lucas, L. Mauger, J.A. Muñoz, Y. Xiao, A.O. Sheets, S.L. Semiatin, J. Horwath, Z. Turgut, Magnetic and vibrational properties of high-entropy alloys, Journal of Applied Physics 109(07E307) (2011).
- [53] B. Feng, M. Widom, Elastic stability and lattice distortion of refractory high entropy alloys, Materials Chemistry and Physics 210 (2017) 309-314.
- [54] O. Delaire, I.I. Al-Qasir, J. Ma, A.M. dos Santos, B.C. Sales, L. Mauger, M.B. Stone, D.L. Abernathy, Y. Xiao, M. Somayazulu, Effects of temperature and pressure on phonons in FeSi1–xAlx, Physical Review B 87(184304) (2013).
- [55] M.S. Lucas, J.A. Muñoz, L. Mauger, C.W. Li, A.O. Sheets, Z. Turgut, J. Horwath, D.L. Abernathy, M.B. Stone, O. Delaire, Y. Xiao, B. Fultz, Effects of chemical composition and B2 order on phonons in bcc Fe–Co alloys, Journal of Applied Physics 108(023519) (2010).
- [56] E. Burkel, Phonon spectroscopy by inelastic x-ray scattering, Reports on Progress in Physics 63(2) (2000) 171-232.
- [57] M.S. Lucas, G.B. Wilks, L. Mauger, J.A. Muñoz, O.N. Senkov, E. Michel, J. Horwath, S.L. Semiatin, M.B. Stone, D.L. Abernathy, E. Karapetrova, Absence of long-range chemical ordering in equimolar FeCoCrNi, Applied Physics LEtters 100(251907) (2012).
- [58] L.K. Béland, G.D. Samolyuk, R.E. Stoller, A. Caro, Lattice thermal conductivity of multi-component alloys, Journal of Alloys and Compounds 648 (2015) 408 -413.
- [59] T. Diaz de la Rubia, R.S. Averback, R. Benedek, W.E. King, Role of Thermal Spikes in Energetic Displacement Cascades, Physical Review Letters 59(17) (1987) 1930-1933.
- [60] J. Dabrowa, M. Zajusz, W. Kucza, G. Cieslak, K. Berent, T. Czeppe, T. Kulik, M. Danielewski, Demystifying the sluggish diffusion effect in high entropy alloys, Journal of Alloys and Compounds 783 (2019) 193-207.
- [61] K.Y. Tsai, M.H. Tsai, J.W. Yeh, Sluggish diffusion in Co–Cr–Fe–Mn–Ni high-entropy alloys, Acta Materialia 61(13) (2013) 4887-4897.
- [62] S. Zhao, T. Egami, G.M. Stocks, Y. Zhang, Effect of d electrons on defect properties in equiatomic NiCoCr and NiCoFeCr concentrated solid solution alloys, Physical Review Materials 2(1) (2018) 013602.
- [63] W.Y. Chen, N. Hashimoto, M.A. Kirk, J.W. Yeh, In-situ Observation of Irradiation Effects on High Entropy Alloys, 316H Stainless Steels and Nickel at 500-700°C, MiNES 2019 Conference Proceedings (2019).
- [64] E. Zarkadoula, G. Samolyuk, W.J. Weber, Two-temperature model in molecular dynamics simulations of cascades in Ni-based alloys., Journal of Alloys and Compounds 700 (2017) 106-112.
- [65] K.C. Russell, R.W. Powell, Dislocation loop nucleation in irradiated metals, Acta Metallurgica 21(3) (1973) 187-193.
- [66] W. Song, T. Ingendahl, W. Bleck, Control of Strain Hardening Behavior in High-Mn Austenitic Steels, Acta Metallurgica Sinica 27(3) (2014) 546-556.
- [67] O.A. Zambrano, Stacking Fault Energy Maps of Fe–Mn–Al–C–Si Steels: Effect of Temperature, Grain Size, and Variations in Compositions, Journal of Engineering Materials and Technology 138(4) (2016).
- [68] S. Zhao, Fluctuations in stacking fault energies improve irradiation tolerance of concentrated solid-solution alloys, Journal of Nuclear Materials (2019).
- [69] J. Ding, Q. Yu, M. Asta, R.O. Ritchie, Tunable stacking fault energies by tailoring local chemical order in CrCoNi medium-entropy alloys, Proceedings of the National Academy of Sciences of the United States of America 115(36) (2018) 8919-8924.

Appendix A1. Microstructural Evolutions with Dpa

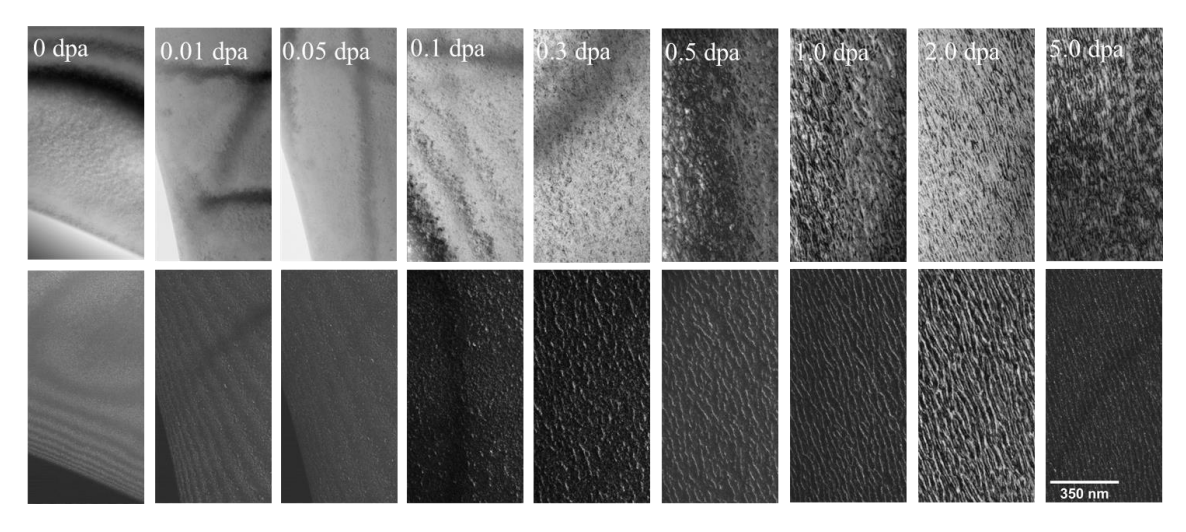


Figure A.1 Microstructural evolution with dpa in $Cr_{18}Fe_{27}Mn_{27}Ni_{28}$ CSA irradiated at 50 K. Top: bright field near z=<111>, Bottom: WBDF g220. Scales are all the same as bottom-right corner.

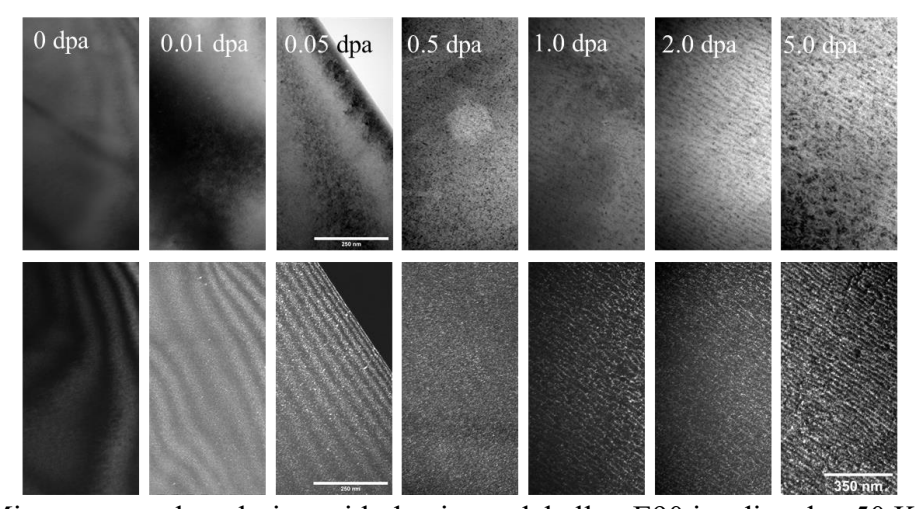


Figure A.2 Microstructural evolution with dpa in model alloy E90 irradiated at 50 K. Top: bright field near z=<111>, Bottom: WBDF g220. Scales are all the same as bottom-right corner except for 0.05 dpa.

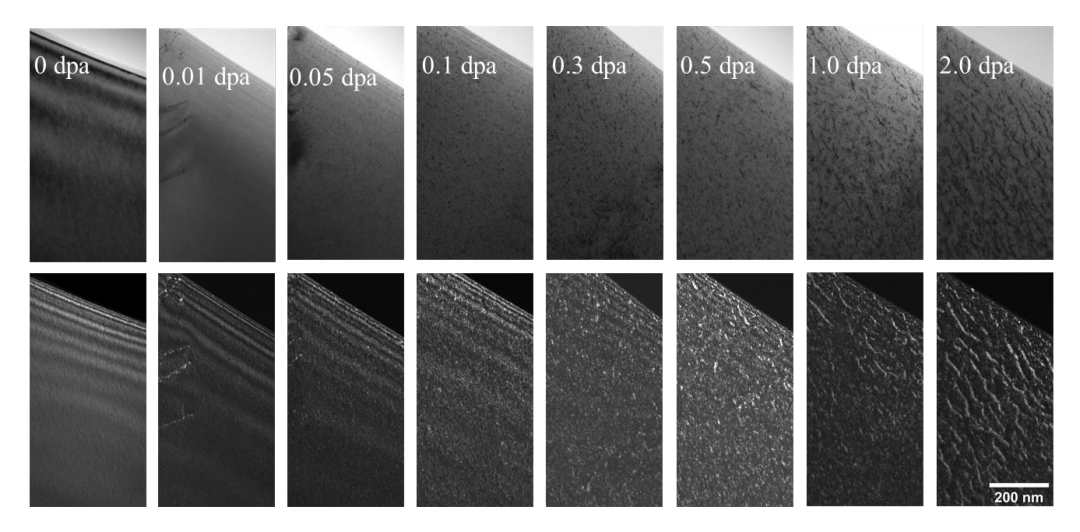


Figure A.3 Microstructural evolution with dpa in $Cr_{15}Fe_{35}Mn_{15}Ni_{35}$ irradiated at 50 K. Top: bright field near z=<011>, Bottom: WBDF g200. Scales are all the same as bottom-right corner.

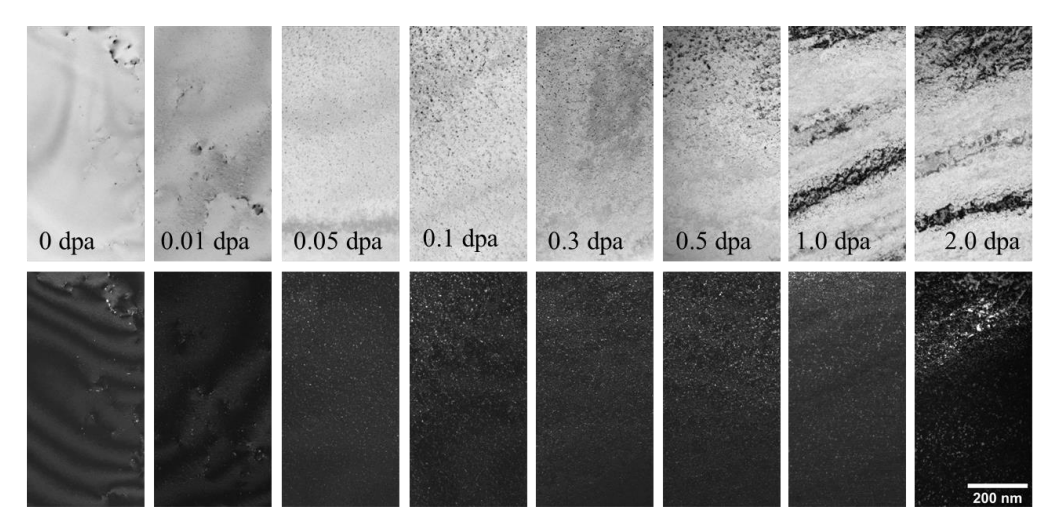


Figure A.4 Microstructural evolution with dpa in pure Ni irradiated at 50 K. Top: bright field near z=<011>, Bottom: WBDF g200. Scales are all the same as bottom-right corner.

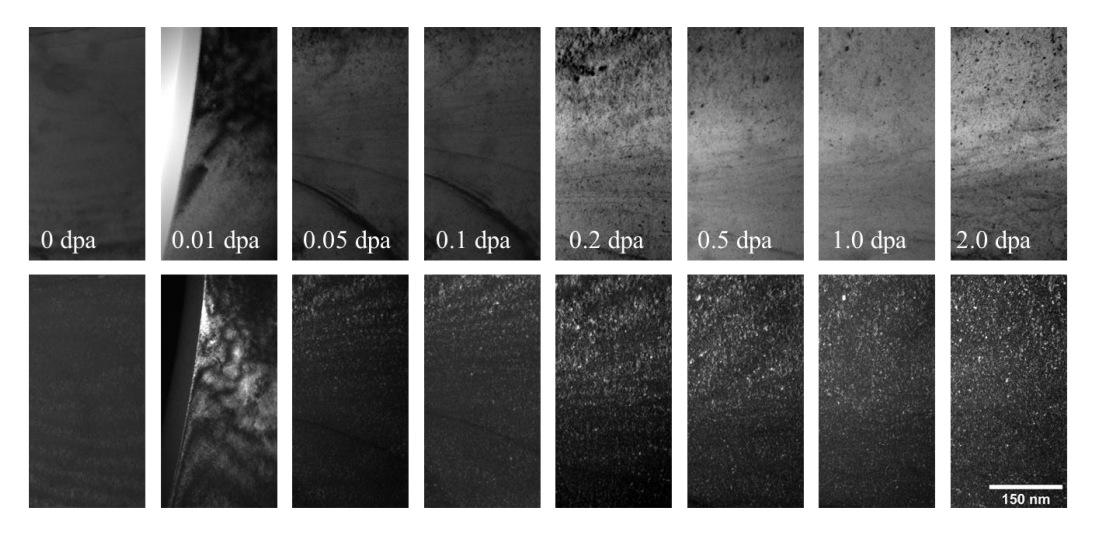


Figure A.5 Microstructural evolution of NbTaTiV during irradiation at 50 K. Top: bright field near z=<111>, Bottom: WBDF g110. Scales are all the same as Bottom-right corner.

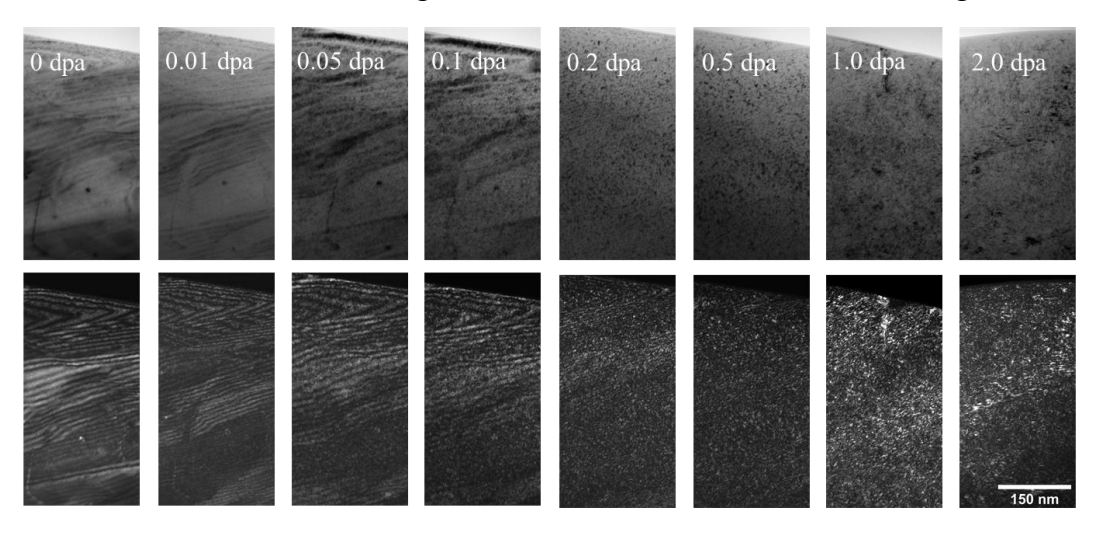


Figure A.6 Microstructural evolution of pure V during irradiation at 50 K. Top: bright field near z=<111>, Bottom: WBDF g110. Scales are all the same as Bottom-right corner.

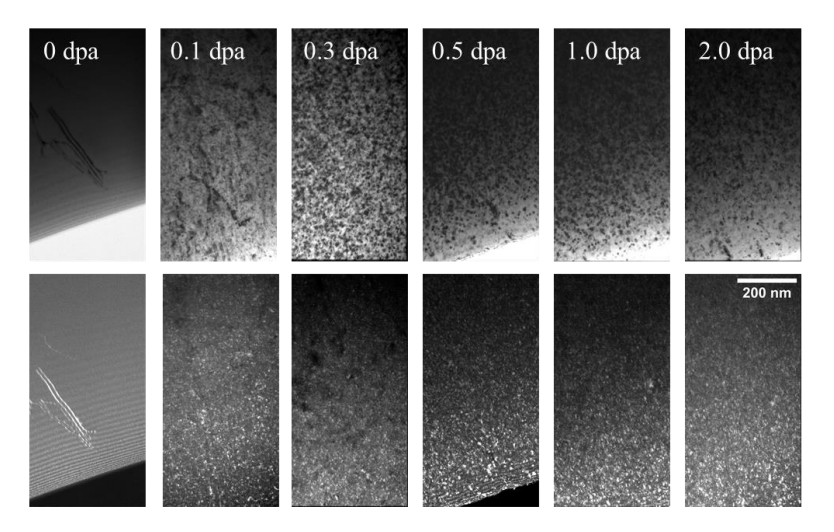


Figure A.7 Microstructural evolution of Cr₁₅Fe₃₅Mn₁₅Ni₃₅ during irradiation at 773 K. Top: bright field near z=<011>, Bottom: WBDF g200. Scales are all the same as bottom-right corner.

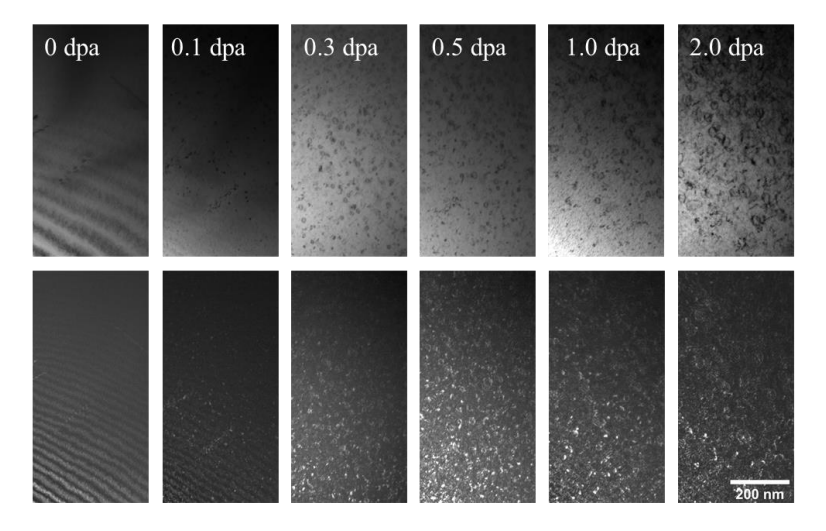


Figure A.8 Microstructural evolution of $Cr_{18}Fe_{27}Mn_{27}Ni_{28}$ during irradiation at 773 K. Top: bright field near z=<011>, Bottom: WBDF g200. Scales are all the same as bottom-right corner.